Acta Materialia 182 (2020) 10–17

Contents lists available at ScienceDirect

Acta Materialia

journal homepage: www.elsevier.com/locate/actamat

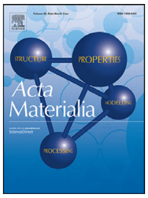

Full length article

Multi-layered domain morphology in relaxor single crystals with nano-patterned composite electrode

Chengtao Luo[a,*], Wei-Yi Chang[a], Min Gao[b], Chih-Hao Chang[a], Jiefang Li[b], Dwight Viehland[b], Jian Tian[c], Xiaoning Jiang[a,*]

[a] *Department of Mechanical and Aerospace Engineering, North Carolina State University, Raleigh, NC 27695, USA*
[b] *Department of Materials Science and Engineering, Virginia Tech, Blacksburg, VA 24061, USA*
[c] *CTS Corporation, 4925 Indiana Ave, Lisle, IL 60532, USA*

ARTICLE INFO

Article history:
Received 18 July 2019
Revised 30 September 2019
Accepted 7 October 2019
Available online 24 October 2019

Keywords:
Piezoelectricity
Domain engineering
Single crystal
Piezoresponse force microscopy (PFM)
Ferroelectric relaxor

ABSTRACT

$(1\text{-}x)\mathrm{Pb(Mg_{1/3}Nb_{2/3})O_3}\text{-}x\mathrm{PbTiO_3}$ (PMN-PT) single crystals, especially with compositions near its morphotropic phase boundary (MPB), have been employed for a broad range of applications such as ultrasound transducers, sensors, and actuators. To further enhance the properties of PMN-PT, electrode patterning, as a method of domain engineering, was proved to be an effective approach. In our previous report, a 200 nm grating pattern electrode (Ti/Au–MnO_x) (nano-electrode) was prepared on one surface of PMN-PT crystal, exhibiting 30% d_{33} enhancement. In this work, the multi-layered domain morphology and the domain engineering from nano-electrode were characterized using piezoresponse force microscopy (PFM). A hypothetical domain engineering model for nano-electrodes is established to explain the experimental results as well as the property enhancement from the nano-electrode. The electrode patterning proves that the nano-scale modification can tune the macro-scale piezoelectric properties of the bulk material.

© 2019 Acta Materialia Inc. Published by Elsevier Ltd. All rights reserved.

1. Introduction

Ferroelectric relaxor-$\mathrm{PbTiO_3}$ single crystals have been extensively studied for their outstanding piezoelectric properties over the last two decades. These materials, such as binary $\mathrm{Pb(Mg_{1/3}Nb_{2/3})O_3–PbTiO_3}$ (PMN-PT), $\mathrm{Pb(Zn_{1/3}Nb_{2/3})O_3–PbTiO_3}$ (PZN-PT) and ternary $\mathrm{Pb(In_{1/2}Nb_{1/2})O_3–Pb(Mg_{1/3}Nb_{2/3})O_3–PbTiO_3}$ (PIN-PMNPT) single crystals with morphotropic phase boundary (MPB) compositions, show excellent properties and have a broad range of applications including next-generation electromechanical devices [1–5].

In relaxor-PT single crystals, domain engineering has proven to be an essential method for enhancing the piezoelectric properties. The relationship between piezoelectric properties and domain morphology was first studied in $\mathrm{BaTiO_3}$ by Wada et al. [6], where a high domain wall density was reported suggesting a large stored mechanical energy density in the boundaries. As predicted by the adaptive phase theory [7], the stored mechanical energy can be mitigated if the twin wall energy is small, and/or if the twin distribution is altered to achieve geometric invariant conditions that relax the elastic energy. The enhanced piezoelectric properties of the monoclinic (M) phase of relaxor-PT crystals are believed to be due to polarization rotation, which requires that the polar anisotropy be small, which in turn requires the twin wall energy to be small. This is true for ***ab-initio*** uniform homogeneous intermediate M phases, and for nonuniform adaptive monoclinic phases consisting of the tiling of polar nanoregions (PNRs). Thus, it is essential to make the domain engineering through the PNRs for the property enhancement, and usually it is achieved by doping during the crystal growing [8].

To shorten the research cycle and reduce the development cost, many new domain engineering methods without changing the composition are also developed, including tuning poling conditions and using patterned electrodes [9]. A domain engineering method that involves patterned electrodes on a perovskite material, $\mathrm{BaTiO_3}$, was studied by Wada et al. [10]. It was reported that the patterned electrode (with a pitch of a few microns) prepared by photolithography could induce finer engineered domain configurations compared to the samples with conventional plane electrodes (plane-electrode). The smaller domain size, corresponding to higher piezoelectric coefficient d_{31} values of $\mathrm{BaTiO_3}$ was also confirmed. Later, another patterned electrode applied on PMN-PT single crystals was reported by Yamashita et al. [11]. In his work, a randomly distributed MnO_x pattern was prepared by sol–gel forming of an Au–MnO_x composite electrode. PMN-28%PT single crys-

---

[*] Corresponding authors.
E-mail addresses: cluo@ncsu.edu (C. Luo), xjiang5@ncsu.edu (X. Jiang).

https://doi.org/10.1016/j.actamat.2019.10.017
1359-6454/© 2019 Acta Materialia Inc. Published by Elsevier Ltd. All rights reserved.

tals with such double-sided electrodes had nearly a 40% improvement in their piezoelectric coefficient (d_{33}). Although this method had the drawbacks of sample electrode pattern randomness and the domain engineering mechanism was not clearly understood, patterned electrodes on relaxor-PT crystals have proven to be an effective domain engineering method.

Recently, PMN-30%PT crystals with nanolithography Ti/Au–MnO_x nano-composite electrodes (nano-electrode, with a pitch of $\sim$ 800 nm) showed high piezoelectric constants of 2250 pm/V and dielectric constants of 6820 at 1 kHz, which represent 36% and 38% enhancements from their conventional plane-electrode counterparts, respectively [12]. The new nano-electrodes were fabricated using Lloyd's mirror interference lithography (LIL), which has the advantages of low cost and high scalability. The necessity of heat treatment mentioned in previous work of Yamashita et al. [11] was proven by time-of-flight secondary ion mass spectrometry (ToF-SIMS), showing that the Mn from MnO_x was diffused into the surface region of PMN-PT crystals during the heat treatment. The inner-bias field observed from P–E loops further confirmed such surface Mn-doping. The influence of nano-electrodes on the local electric field was further simulated by COMSOL, showing the strong localized non-uniform electric fields on the edge of each MnO_x nanograting, or fringe effect. The simulation result was then used to explain the domain morphology on the (001) plane according to a previously reported model from a $LiNbO_3$ study [13], which pointed out that domain engineering may originate from spatially non-uniform fields. However, further piezoresponse force microscopy measurements (PFM) revealed that the domain morphology did not follow the orientation of the nano-electrode when the sample thickness was $\geq$200 µm [12], which was not shown in the case of $LiNbO_3$ [13,14]. More evidence from X-ray diffraction (XRD) reciprocal space mapping (RSM) was provided by Gao's et al. work recently [15]. The lattice symmetry from near-surface regions clearly showed the field-induced rhombohedral (R) – monoclinic (M_A) phase transition, while the detailed RSM patterns further proved the existence of the non-uniform poling fields underneath the nano-electrode. At the same time, the difference between the XRD results from the nano-electrode and plane-electrode calls for a suitable heterogeneous domain engineering model to integrate these findings based on the domain morphologies.

In this study, we advanced the study of poled PMN-30%PT with Ti/Au–MnO_x nano-composite electrodes (nano-electrode) [12,16] by focusing on the measurement of domain morphology. The domain patterns on the cross-section plane were found changing from near-surface to interior regions, forming multi-layered domain morphologies. By comparing the domain densities and region boundaries within the domain morphology of nano-electrode and plane-electrode crystals, the polarization rotation sequences were determined and the domain engineering from the nano-electrode was explained. The nano-electrode confined the monoclinic in the near-surface region and block the interior polarization rotation, and the resulting overall rising of the stored mechanical energy was the key to the property enhancements.

2. Experimental procedure

2.1. Fabrication of nano-electrode samples

The tested samples in this work were the [001]-grown PMN-30%PT single crystals (CTS Corporations, IL, USA). The original single crystal wafer was [001]-orientated and had the dimension of $20 \times 20 \times 0.6\,mm^3$. The one-sided nano-electrode was fabricated on one $20 \times 20\ mm^2$ side before the wafer was diced into [001]-orientated rectangular plates ($4 \times 4 \times 0.6\,mm^3$) for experiments.

Same to our previous works [12,16], Lloyd's mirror interference lithography (LIL) was used in nano-electrode fabrication. In general, LIL is a photolithography technique widely used in nanograting structure fabrication, which is sufficient for controlling nanostructure sizes on a large exposure area. The distance between the nanograting, or grating period, or the pitch size we used in this work was 500 nm. The Mn films were deposited and patterned nanogratings were formed along the [100] direction. A heat treatment (800 °C, 3 h) was then conducted to further introduce the doping of Mn into the surface. In the end, a layer of 5 nm-thick Ti and 100 nm-thick gold was deposited through electron-beam evaporation on the entire top surface of the sample as a nano-electrode. The Ti/Au electrodes were also deposited on the other surface of nano-electrode crystals to create parallel-plate capacitors. Since the tested samples are the same, more detailed fabrication processes can be found in our previous publication [12].

Conventional plane-electrode PMN-30%PT single crystals, as the control group, were prepared with the same dimensions. The same Ti/Au electrode used in the nano-electrode samples were deposited on both sides. The plane-electrode samples were poled at an electric field amplitude of 10 kV/cm for 30 min at room temperature in air.

2.2. PFM measurements

The domain morphology was observed by piezoresponse force microscopy (PFM) (Dimension Icon, Bruker, USA). Before the PFM experiment, the poled $4 \times 4 \times 0.6\,mm^3$ thin plate samples were broke along the [010] direction, and the resulting cross-section (100) plane was perpendicular to the [100]-orientated nanogratings and two electrode surfaces. The necessary electrode isolation was made to prevent the short and the cross-section (100) plane was then scanned under the PFM. Within the description of multi-layered domain morphology in this work, 'depth' was used for referring to the distance between the nano-electrode surface and the point under the PFM scanning. In this work, the depth range of the PFM scanning area was 20–300 µm to protect the PFM probes.

3. Experimental results

Before discussing the detailed PFM results, Fig. 1 schematically shows how to distinguish the different domain configurations according to the PFM contrasts. First, the as-grown PMN-30%PT samples are in the rhombohedral (R) phase [17]. After poling along [001] direction, the R phase has four possible spontaneous polarization directions along $\langle 111 \rangle$, and forms what is designated as the '*4R*' configuration [1] in Fig. 1(a). For PMN-30%PT single crystal, the poling field along [001] direction may also induce the phase transition [18] from R phase to monoclinic A (M_A) phase (the notation M_A follows definitions of Vanderbilt and Cohen [19]). Like the *4R*, the polarization orientations of the monoclinic (M) phase after the phase transition, or polarization rotation, also form a '*4M*' configuration, as illustrated in Fig. 1(a). However, practically, the equivalent polarization direction from the *4R* may not be perfectly aligned along the [001] direction. Thus, the two $\langle 111 \rangle$ polarization vectors may rotate and form the '*2R*' configuration, as shown in Fig. 1(b). Here, the *2R* is still in the [001]-poled condition, which is different from the [011]-poled '*2R*' [1].

Secondly, 71° and 109° domain walls within each domain configuration can be distinguished by PFM measurements. As schematically illustrated in Fig. 1(c), the in-plane PFM phase contrast marked the [0 + q 0] and [0 −q 0] polarization orientations (wavevector q not specified), while the out-plane PFM phase contrast marks the [+q 0 0] and [−q 0 0] ones. Here, the coordinate system orientation used in Fig. 1(c) is also used in describing the following PFM results in this work. By combining these phase contrasts, the *4R* configuration can be obtained, as shown in Fig. 1(d).

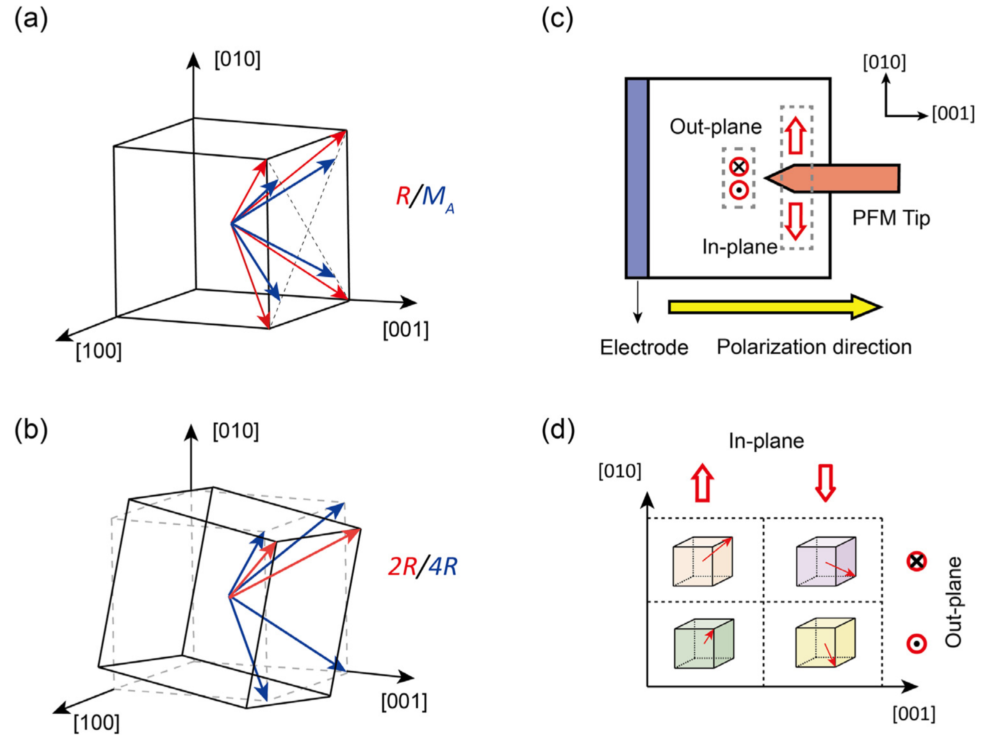

Fig. 1. PFM settings and domain configurations: (a) poled rhombohedral and monoclinic polarization in pseudocubic lattice, (b) *4R* and *2R* domain configurations, (c) nano-electrode sample's orientation during the PFM measurement, marking in-plane polarization is along [010] direction and out-plane polarization is along [100] direction, (d) *4R* configuration from in-plane and out-plane PFM phase contrasts combinations.

In the case of the *2R* in Fig. 1(b), there is no in-plane phase contrast, so the corresponding combination number is also halved.

In poled relaxor-PT single crystals, 'skin effects' are usually used to describe the lattice symmetry difference between XRD and neutron diffraction results on the same sample [20–23]. Considering the penetration and scattered range of the X-rays are much smaller than that of neutron beams, the lattice symmetry has been shown to be different at different depths from the surface of poled crystals. In this study, domain morphologies from both nano-electrode and plane electrode crystals are compared at different depths from the electrode surface. The influence from the poling electric field amplitude upon the domain morphology is also considered.

3.1. Domain morphology from the nano-electrode sample

The domain morphology of the nano-electrode crystal is shown in Fig. 2. Both *4R* and *2R* domain configurations (schematically illustrated in Fig. 1(b)) were observed. The out-plane PFM results are schematically illustrated in Fig. 2(a), which shows that the region with a *2R* domain configuration (*2R* region), is located closer to the nano-electrode surface than the region with a *4R* domain configuration (*4R* region). Fig. 2(a) also demonstrates the difference between the 71° and 109° domain walls. In detail, the *2R* region only has 71° domain walls, whereas the *4R* region has both 71° and 109° domain walls (Fig. 2(b) and (d)). Fig. 2(c) and (e) provide the additional in-plane PFM results taken from the same area as that of Fig. 2(b) and (d), respectively. The depth range is 45–95 μm for Fig. 2(b) and (c), and 166–216 μm for Fig. 2(d) and (e). Generally, domain walls in the *2R* regions show a longer range of polar ordering and larger domain widths, than those in the *4R* regions.

Further experiments, the PFM scanning on the full range of the depth, show that the domain morphology is also related to the poling field amplitudes. In Fig. 3, the *4R* and *2R* regions can be distinguished, and the boundaries between these regions are in the middle of each panel. Fig. 3(a) and (b) shows the same region from a crystal poled under 5 kV/cm. Similarly, Fig. 3(c) and (d) show the same region for a poling field of 7.5 kV/cm. Additionally, the boundary locations are found to shift with different poling electric field amplitudes. The depths of the boundaries are 66.5 μm, 78 μm and 99.5 μm for samples poled under 5 kV/cm, 7.5 kV/cm, and 10 kV/cm, respectively. This shifting can be explained by the local free energy difference between the two regions. Since the *2R* configuration is developed from the *4R* by polarization rotation, as discussed with regards to Fig. 1(b), the free energy of the *2R* regions is lower than *4R* ones. Such an energy difference is higher in a larger poling field and thus the *4R*→*2R* transition becomes easier, making the *2R* region broader. It can also be concluded that this kind of domain configuration transition happens from the electrode surface to interior regions. For finer domain scales, the 71° domain density in the *2R* region is highly dependent on the poling field amplitude, whereas the domains in the *4R* region show little changes. The detailed statistics on domain widths will be further discussed in the later chapter.

3.2. Domain morphology from the plane-electrode crystals

The domain morphology of the plane-electrode crystal is shown in Fig. 4. Like Fig. 2(a), a schematic illustration of the domain patterns is given in Fig. 4(a). Comparing to the nano-electrode samples, the plane-electrode ones have a remarkable extra region between the electrode surface and the *2R* region. To determine the domain configuration of this region, both reported XRD results [15] and PFM results in this work are considered. First, the skin effect was observed in PMN-30%PT single crystal [20], and the lattice symmetry of the near-surface region was confirmed as M_A phase in the recent XRD reports [15]. Secondly, PFM results in Fig. 4(b) and (c) show that the extra region has observable longitudinal 109° domain walls, while the 71° domain walls are only partially distributed and not recognizable in most areas. Thus, the in-plane and out-plane contrast combination number is two in the most

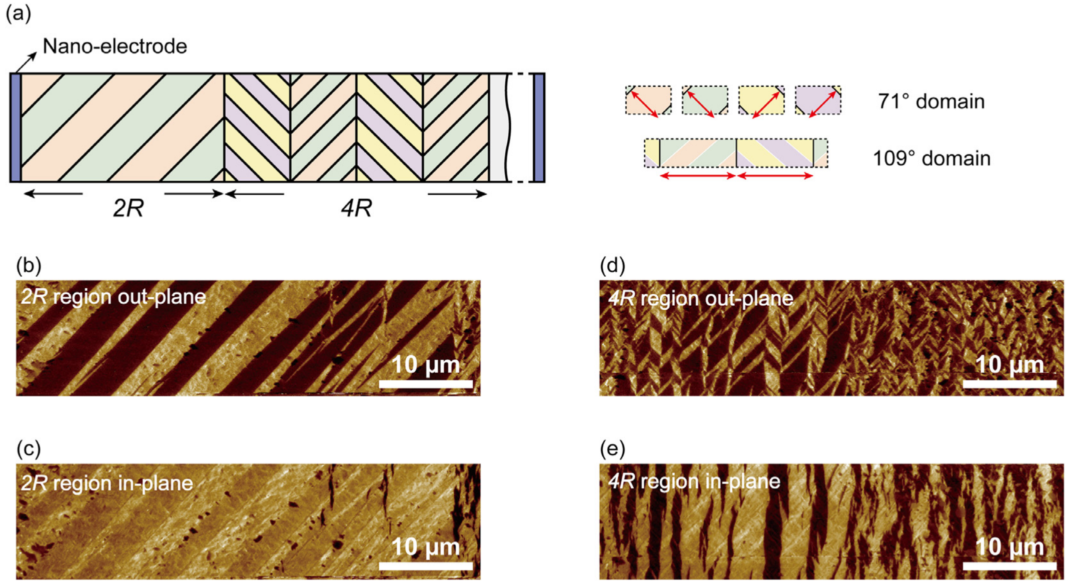

Fig. 2. Domain morphology from the nano-electrode sample poled under 10 kV/cm. (a) The schematic domain patterns in the (100) plane show the *2R*→*4R* region sequence near the nano-electrode. PFM results are separately shown as (b) out-plane domain pattern in *2R* region, (c) in-plane domain pattern in *2R* region, (d) out-plane domain pattern in *4R* region, and (e) in-plane domain pattern in *4R* region.

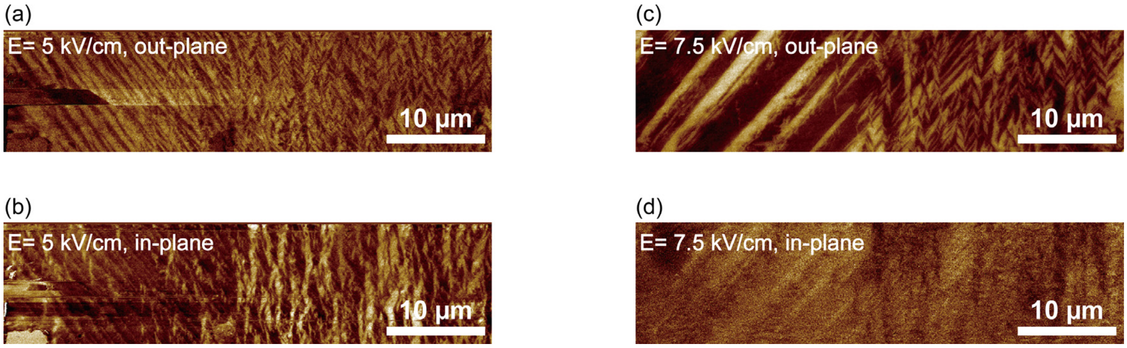

Fig. 3. Domain morphology in the (100) plane with *2R*→*4R* region boundaries from the nano-electrode samples. PFM results are separately shown as (a) out-plane domain pattern poled under 5 kV, (b) in-plane domain pattern poled under 5 kV, (c) out-plane domain pattern poled under 7.5 kV, and (d) in-plane domain pattern poled under 7.5 kV.

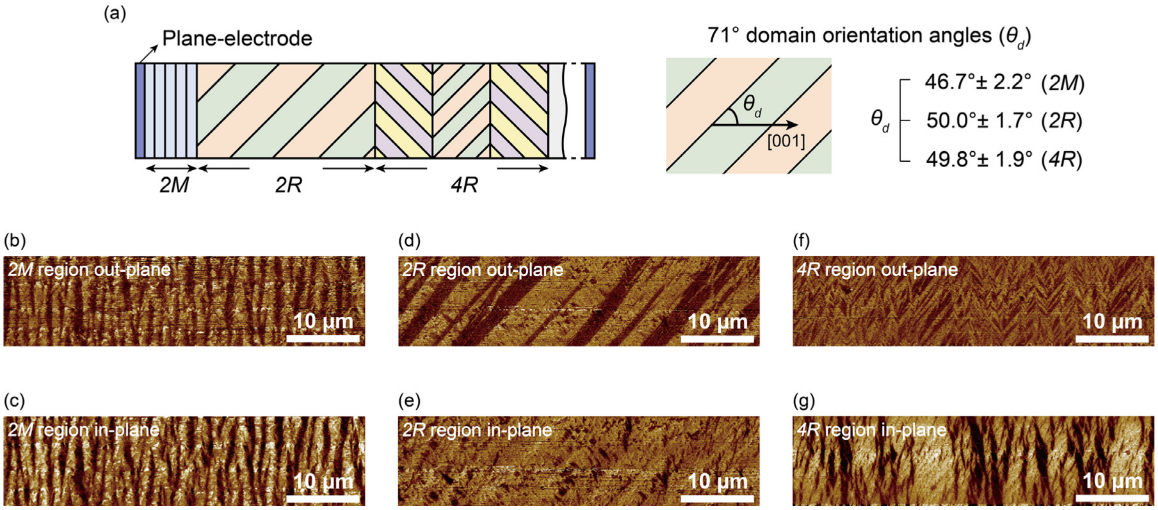

Fig. 4. Domain morphology from the plane-electrode sample poled under 10 kV/cm. (a) The schematic domain patterns in the (100) plane show the *2M*→*2R*→*4R* region sequence near the plane-electrode. The 2 M region just marks the vertical 109° domain wall. The 71° domain wall orientation angle (θ_d) from different regions are also listed. PFM results are separately shown as (b) out-plane domain pattern in 2 M region, (c) in-plane domain pattern in 2 M region, (d) out-plane domain pattern in *2R* region, (e) in-plane domain pattern in *2R* region, (f) out-plane domain pattern in *4R* region, and (g) in-plane domain pattern in *4R* region.

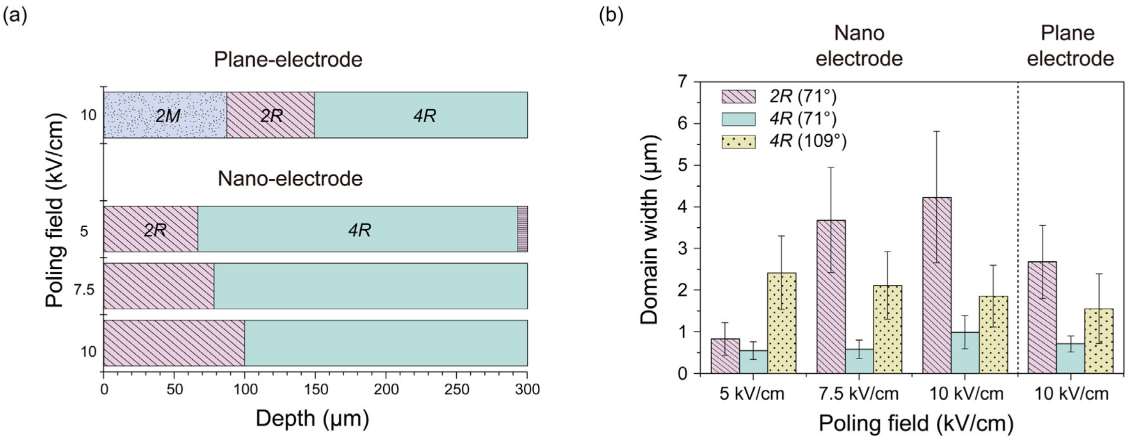

Fig. 5. Statistics of domain morphology from both nano-electrode and plane-electrode crystals in different poling fields. (a) Region boundaries from different samples in different poling conditions; (b) domain width of the nano-electrode crystals in different poling conditions with the comparison of the plane-electrode one.

part of this extra region and brings the '*2M*' domain configuration which can summarize the features from both XRD and PFM results. (The partially distributed 71° domain walls in *2M* region is further shown in **Fig. S1**.)

As shown in Fig. 4(a), the 71° domain orientation angles (θ_d) are measured relative to the horizontal [001] direction. Fig. 4(a) also lists the θ_d from *2M, 2R* and *4R* regions. The measured 71° domain walls are chosen from randomly picked areas where the in-plane contrasts are the same to make $0^\circ < \theta_d < 90^\circ$. The statistical results show that the 71° domain walls are tilted toward to [001] direction (θ_d is decreased) by about 3° from *2R* region to 2*M* region, while θ_d is consistent from *4R* region to *2R* region. The measured θ_d decreasing here corresponds to the $R \rightarrow M_A$ phase transition, while the same polarization rotation was already proved by XRD result before [18,24].

In addition to the *2M* region shown in Fig. 4(b) and (c), the *2R* and *4R* regions are also shown in Fig. 4. Like Fig. 2 and Fig. 3, the in-plane and out-plane results of Fig. 4 have the same depth ranges: 25–75 µm (Fig. 4(b) and (c)), 115–165 µm (Fig. 4(d) and (e)), and 202–252 µm (Fig. 4(f) and (g)). Similar to Fig. 3, the domain morphology including the region boundaries are provided in **Fig. S2**, showing both *2M* → *2R* and *2R* → *4R* region boundaries.

3.3. Domain statistics

The statistical results of domain morphology from PFM results are summarized in Fig. 5. The effects of different electrode types and poling field amplitudes are both considered. The counted PFM data is including but not limited to those previously given in Figs. 2–4.

First, the multi-layered domain morphologies which are marked by different domain configuration types are shown in Fig. 5(a). The region boundary locations are also compared in different samples. Generally, the plane-electrode crystals have *2M, 2R, 4R* regions from the electrode surface to the interior, whereas the nano-electrode crystal only has *2R* and *4R* regions and is not fully poled under 5 kV/cm. A near-linear movement of the *2R* → *4R* boundary is observable with increasing poling field.

Meanwhile, the domain width from both 71° and 109° domains are compared in Fig. 5(b). As it is shown in the right part of Fig. 2(a), the 71° domain width is calculated from the out-plane contrasts, while the 109° domain width is mainly calculated from the in-plane contrasts. The calculated domains are randomly chosen in different depths, while the domain width is not changing with the depth within each region. Thus, the domain width from different regions can be summarized without the depth information in Fig. 5(b). With increasing poling field, the 71° domains from both the *2R* and *4R* regions become broader, whereas those from the *2R* regions grow significantly. Such morphology differences indicate that the stored mechanical energy in the 71° domain wall is decreased in the *2R* → *4R* crossover, as the polarization is increased. On the other hand, the 109° domain width is not sensitive to the poling field, as 109° polarization rotation requires more energy than the 71° ones. Secondly, the domain width from plane-electrode crystals is shown in the right part of Fig. 5(b). Under a poling field of 10 kV/cm, instead of forming *2M* regions, the *2R* region domains in the nano-electrode sample is broader than those in the plane-electrode one.

From the view of domain engineering [1,9], the enhancement of the domain density (reciprocal of domain width) is the key origin of understanding the piezoelectric property enhancement. Compared to plane-electrode crystals, the nano-electrode ones have wider *4R* regions (Fig. 5(a)). Moreover, the domain density of the *4R* regions is the highest amongst all types of regions. Since the *2R* region has no 109° domain wall and *2M* region has little 71° domain wall, the volume fraction of the *4R* region greatly affect the total domain density. Thus, although the single domain width is slightly higher (in *4R* region) in the nano-electrode crystals than in the plane-electrode ones (Fig. 5(b)), the total domain density is still higher in the nano-electrode crystals than in the plane-electrode ones, which contributes to their piezoelectric property enhancement. The significant 71° domain wall merging in the nano-electrode crystal (Fig. 5(b)) will be further discussed from the energy view later in this work.

3.4. Lattice symmetry from the surface of the plane-electrode sample

In Fig. 5(a), the most significant difference in the lattice symmetry is the existence of the extra *2M* region in the plane-electrode sample. However, it cannot be concluded that there is no *M* phase in the nano-electrode sample, since the lattice symmetry from the near-surface region (depth < 20 µm) cannot be provided by PFM scanning. The PFM probes are easily broken in this region because of the sample topography near the edge changes rapidly and randomly. To solve this problem, *in-situ* XRD was used to scan the lattice symmetry from the near-surface region under the nano-electrode (depth < 10 µm [24,25]). These results were published in our previous report of Gao et al. [15]. Here, XRD RSM from (002) zone was provided in **Fig. S3**. The XRD/PFM result difference indicates that the *M* phase domains in the nano-electrode crystal are confined to the near-surface regions. So, the multi-layered domain morphologies for both nano-electrode and

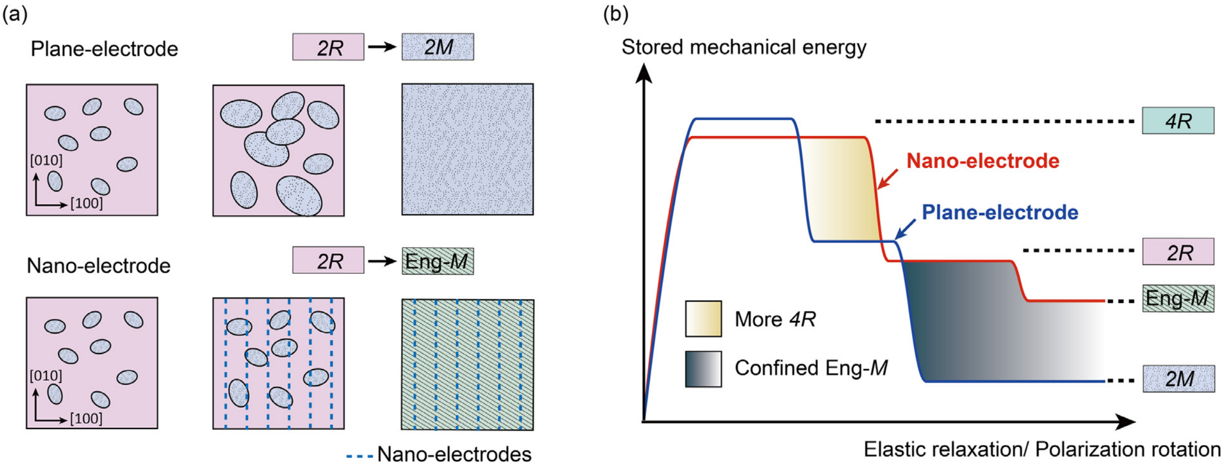

Fig. 6. The schematic processes of domain engineering from both plane-electrode and nano-electrode: (a) The *M* phase domain growth in the (001) plane near-surface region during the field-induced phase transition; (b) The stored mechanical energy changes with the increasing polarization in the near-surface region.

plane-electrode sample from the near-surface to interior region are both $M \rightarrow 2R \rightarrow 4R$, while *M* phase conditions from samples with different electrode types are different in the randomness and depth distribution ranges.

4. Domain engineering model for nano-electrode

A suitable domain engineering model is hypothesized to interpret the multi-layered domain morphologies based on PFM and XRD results. The schematic process of the domain engineering from both plane-electrode and nano-electrode crystals are illustrated (Fig. 6) from views of domain growing process in the (001) plane near-surface region (Fig. 6(a)) and changes on stored mechanical energy (Fig. 6(b)). In the case of the plane-electrode crystal, from left to right in Fig. 6(a), the new *M* phase domains grow and occupy the whole surface after the phase transition. The near fully relaxed *M* phase domains merge and form the *2M* region near the surface. In comparison, the growth of the new *M* phase domains in the nano-electrode crystal is confined by the Mn ions from the nano-electrodes. Such influence is represented by the dashed lines in Fig. 6(a), and further PFM images (see **Fig. S4**) proves that the final engineered domain structure follows the shape and orientation of the nano-electrodes. The Mn-dopant in the relaxor-PT usually behaves as acceptors, inducing oxygen vacancies and forming defect dipoles. This, in turn, pins the domain wall motion and polarization rotation [26–28]. Such pinning effects result in nonuniform *M* phase with high randomness and poor short-range-ordering. Such high domain wall randomness was proved independently from the XRD peaks splitting and broadening in our previous XRD report [15].

From an energy perspective as shown in Fig. 6(b), the confined *M* phase region continues affecting the domain configuration transitions at different depths and different degrees of elastic relaxation. Since an $R \rightarrow M$ phase transition was proved in the XRD result [15], the polarization rotation end of the nano-electrode sample is marked as engineered *M* phase (Eng-*M)* to distinguish from the relaxed *2M* region of the plane-electrode sample. As the net polarization increases, the mechanical energy is transferred into an electrical one. The plane-electrode crystal has a *4R→2R→2M* domain configuration transition sequence (blue line) with decreasing stored elastic energy, whereas the nano-electrode (red line) had a *4R→2R→*Eng-*M* one. According to the adaptive phase theory [7], the unrelaxed mechanical energy stored in the near-surface regions is higher than that fully relaxed one in *2M* region of the plane-electrode sample. Considering the previous domain statistic, in Fig. 6(b), the stored energy levels have an increasing order of *2M-(*Eng-*M)–2R*(nano-electrode)*–2R*(plane-electrode)*–4R*. Thus, the total stored energy increasing from plane-electrode to nano-electrode is mainly contributed into two parts: one is the wider *4R* region and one is the confined Eng-*M* region, both marked by the shadow areas in Fig. 6(b). These two factors are also two main origins of the nano-electrode property enhancement.

Moreover, the *4R→2R→2M* domain configuration transition sequence in the near-surface region is the origin of the *2M→2R→4R* region sequence in Fig. 5(a), showing that the polarization rotations of the interior region are later than those from the near-surface region. Such heterogeneous domain relaxation in different depths/regions explains the significant 71° domain wall merging in nano-electrode crystal, as shown in Fig. 5(b). Since the mechanical energy relaxation through *2R→2M* rotation is blocked or confined in the near-surface region of the nano-electrode crystal, the domain wall merging instead of polarization rotation is becoming a dominating way to lower the system free energy in the interior *2R/4R* regions. Thus, the single domain widths are higher in the nano-electrode crystal than those in the plane-electrode ones.

Previously reported P–E loops showed that the coercive field (E_C) of the nano-electrode crystals (E_C is about 2.24 kV/cm) was nearly unchanged with respect to plane-electrode samples (2.45 kV/cm) [12], which is unique compared to other Mn-doped relaxor-PT results [1,9,29]. Mn-doping is widely used to raise the mechanical quality factor and the Curie temperature, and the doped relaxor-PT properties generally become harder (larger E_C) with lower d_{33} values [29]. Such differences between Mn-doped and the nano-electrode relaxor-PT crystals indicate a contrast in the Mn ion distributions between the two cases. In the nano-electrode crystals, Mn ions diffusing in from the nano-electrode are only located in the near-surface region [12]. Thus, the heterogeneous poling model above describes a possible role for the Mn-doping, which can prevent polarization rotation in the interior region and maintain a high domain wall density in the volume.

This hypothesized model indicates that such a domain engineering method has much potential with regards to countering scaling effects in PMN-PT crystals. Scaling effects have been reported showing that the dielectric and electromechanical properties degrade with decreasing thickness [1,28,30–33], associated with a decrease in the ferroelectric domain size. Here, a higher total domain wall density (or smaller domain size) was found in the nano-electrode crystals, compared to the conventional plane-electrode ones. In addition, the domain engineering for the nano-electrode crystals begins from the near-surface region (<20 μm), and thus the domain engineering introduced by the nano-electrode will still be effective with decreasing crystal thickness, preventing significant property decrements ($<200\,\mu m$ [33]). Accordingly, nano-electrodes and their unique domain engineering will be effective in mitigating scaling effect problems.

5. Conclusion

PMN-30%PT single crystals with a one-side nano-electrode have been reported to have up to a 30% enhancement in their d_{33} value. Here, a study was made to further explain the property enhancement from the perspective of nano-electrodes using domain engineering.

Both nano-electrode and plane-electrode poled crystals were characterized. They had different domain morphologies at different depths from the electrode surfaces to the crystal interiors. The domain region sequence from the surface was found to be *2M*→*2R*→*4R* for the plane-electrode crystal, and Eng-*M*→*2R*→*4R* for the nano-electrode samples. The corresponding domain width statistics showed that total domain wall density was higher in the nano-electrode crystals. The high domain wall density from the wider *4R* region of the nano-electrode crystals is an essential origin of the property enhancement. In addition, the *M* phase domain engineered by the nano-electrode were found to have higher randomness compared to the plane-electrode ones. According to the adaptive phase theory, the corresponding higher stored elastic energy is essential to property enhancement.

In summary, a suitable domain engineering model is hypothesized to interpret the multi-layered domain morphologies based on PFM and XRD results. The electrode patterning proves that the nano-scale modification can tune the macro-scale piezoelectric properties of the bulk material from the electrode surface. Thus, this domain engineering method has much potential to counter scaling effects in relaxor-PT crystals and has a promising prospect in the future developments of microelectromechanical systems (MEMS).

Declaration of Competing Interest

The authors declare that they have no known competing financial interests or personal relationships that could have appeared to influence the work reported in this paper.

Acknowledgment

This work was supported by ONR under Grant #N00014-15-1-2418 and N00014-18-1-2538. This work was performed in part at the Analytical Instrumentation Facility (AIF) at North Carolina State University, which is supported by the State of North Carolina and the National Science Foundation (award number ECCS-1542015). The AIF is a member of the North Carolina Research Triangle Nanotechnology Network (RTNN), a site in the National Nanotechnology Coordinated Infra- structure (NNCI). The work at Virginia Tech was supported by ONR under Grant # N00014-17-1-2234.

Supplementary material

Supplementary material associated with this article can be found, in the online version, at doi:10.1016/j.actamat.2019.10.017.

References

[1] S.J. Zhang, F. Li, X.N. Jiang, J. Kim, J. Luo, X.C. Geng, Advantages and challenges of relaxor-PbTiO3 ferroelectric crystals for electroacoustic transducers – a review, Prog. Mater. Sci. 68 (2015) 1.

[2] J. Ma, K. Martin, P.A. Dayton, X. Jiang, A preliminary engineering design of intravascular dual-frequency transducers for contrast-enhanced acoustic angiography and molecular imaging, IEEE Trans. Ultrason. Ferroelectr. Freq. Control 61 (2014) 870.

[3] X.N. Jiang, J. Kim, K. Kim, F-PT single crystal piezoelectric sensors, Crystals 4 (2014) 351.

[4] S.E. Park, T.R. Shrout, Relaxor based ferroelectric single crystals for electro-mechanical actuators, Mater. Res. Innov. 1 (1997) 20.

[5] S.E.E. Park, W. Hackenberger, High performance single crystal piezoelectrics: applications and issues, Curr. Opin. Solid State Mat. Sci. 6 (2002) 11.

[6] S. Wada, S. Suzuki, T. Noma, T. Suzuki, M. Osada, M. Kakihana, S.E. Park, L.E. Cross, T.R. Shrout, Enhanced piezoelectric property of barium titanate single crystals with engineered domain configurations, Jpn. J. Appl. Phys. 38 (1999) 5505.

[7] D.D. Viehland, E.K.H. Salje, Domain boundary-dominated systems: adaptive structures and functional twin boundaries, Adv. Phys. 63 (2014) 267.

[8] F. Li, D. Lin, Z. Chen, Z. Cheng, J. Wang, C. Li, Z. Xu, Q. Huang, X. Liao, L.Q. Chen, T.R. Shrout, S. Zhang, Ultrahigh piezoelectricity in ferroelectric ceramics by design, Nat. Mater. 17 (2018) 349.

[9] E. Sun, W. Cao, Relaxor-based ferroelectric single crystals: growth, domain engineering, characterization and applications, Prog. Mater. Sci. 65 (2014) 124.

[10] S. Wada, K. Yako, T. Muraishi, K. Yokoh, S.M. Nam, H. Kakemoto, T. Tsurumi, Enhanced piezoelectric property of barium titanate single crystals by domain wall engineering using patterning electrode, Ferroelectrics 340 (2006) 17.

[11] Y. Yohachi, J. John, N. Yamamoto, K. Itsumi, Y. Hosono, Effects of manganese oxides/gold composite electrode on piezoelectric properties of lead magnesium niobate titanate single crystal, Jpn. J. Appl. Phys. 50 (2011) 09NC05.

[12] W.Y. Chang, C.C. Chung, Z.Y. Yuan, C.H. Chang, J. Tian, D. Viehland, J.F. Li, J.L. Jones, X.N. Jiang, Patterned nano-domains in PMN-Pt single crystals, Acta Mater. 143 (2018) 166.

[13] V.Y. Shur, E.L. Rumyantsev, E.V. Nikolaeva, E.I. Shishkin, D.V. Fursov, R.G. Batchko, L.A. Eyres, M.M. Fejer, R.L. Byer, J. Sindel, Formation of self-organized nanodomain patterns during spontaneous backswitching in lithium niobate, Ferroelectrics 253 (2001) 661.

[14] R.G. Batchko, V.Y. Shur, M.M. Fejer, R.L. Byer, Backswitch poling in lithium niobate for high-fidelity domain patterning and efficient blue light generation, Appl. Phys. Lett. 75 (1999) 1673.

[15] M. Gao, C.T. Luo, W.Y. Chang, C.M. Leung, J. Tian, J.F. Li, X.N. Jiang, D. Viehland, Apparent phase stability and domain distribution of PMN-30Pt single crystals with nanograted Au/MnO_x electrodes, Acta Mater. 169 (2019) 28.

[16] W.Y. Chang, W. Huang, A. Bagal, C.H. Chang, J. Tian, P. Han, X. Jiang, Study on dielectric and piezoelectric properties of 0.7 Pb(Mg1/3Nb2/3)O3-0.3 PbTiO3 single crystal with nano-patterned composite electrode, J. Appl. Phys. 114 (2013) 114103.

[17] B. Noheda, D.E. Cox, G. Shirane, J. Gao, Z.G. Ye, Phase diagram of the ferroelectric relaxor (1-*x*)PbMg1/3Nb2/3O3-*x*PbTiO(3), Phys. Rev. B 66 (2002) 054104.

[18] F.M. Bai, N.G. Wang, J.F. Li, D. Viehland, P.M. Gehring, G.Y. Xu, G. Shirane, X-ray and neutron diffraction investigations of the structural phase transformation sequence under electric field in 0.7Pb(Mg1/3Nb2/3)-0.3PbTiO(3) crystal, J. Appl. Phys. 96 (2004) 1620.

[19] D. Vanderbilt, M.H. Cohen, Monoclinic and triclinic phases in higher-order Devonshire theory, Phys. Rev. B 63 (2001) 094108.

[20] D. Phelan, E.E. Rodriguez, J. Gao, Y. Bing, Z.G. Ye, Q. Huang, J. Wen, G. Xu, C. Stock, M. Matsuura, P.M. Gehring, Phase diagram of the relaxor ferroelectric (1 −x)Pb(Mg1/3Nb2/3)O3+xPbTiO3revisited: a neutron powder diffraction study of the relaxor skin effect, Phase Transit. 88 (2015) 283.

[21] B. Dkhil, J.M. Kiat, G. Calvarin, G. Baldinozzi, S.B. Vakhrushev, E. Suard, Local and long range polar order in the relaxor-ferroelectric compounds PbMg1/3Nb2/3O3 and PbMg0.3Nb0.6Ti0.1O3, Phys. Rev. B 65 (2002) 024104.

[22] G. Xu, P.M. Gehring, C. Stock, K. Conlon, The anomalous skin effect in single crystal relaxor ferroelectric PZN-XPT and PMN-XPT, Phase Transit. 79 (2006) 135.

[23] N. Domingo, N. Bagués, J. Santiso, G. Catalan, Persistence of ferroelectricity above the Curie temperature at the surface of Pb(Zn1/3Nb2/3)O3−12%PbTiO3, Phys. Rev. B 91 (2015) 094111.

[24] H. Cao, J.F. Li, D. Viehland, G.Y. Xu, Fragile phase stability in (1-*x*)Pb(Mg1/3Nb2/3O3)-*x*PbTiO(3) crystals: a comparison of [001]and [110]field-cooled phase diagrams, Phys. Rev. B 73 (2006) 184110.

[25] H. Cao, F.M. Bai, N.G. Wang, J.F. Li, D. Viehland, G.Y. Xu, G. Shirane, Intermediate ferroelectric orthorhombic and monoclinic M–B phases in [110]electric–field-cooled Pb(Mg1/3Nb2/3)O-3-30%$PbTiO_3$ crystals, Phys. Rev. B 72 (2005) 064104.

[26] X. Li, X. Zhao, B. Ren, H. Luo, W. Ge, Z. Jiang, S. Zhang, Microstructure and dielectric relaxation of dipolar defects in Mn-doped $(1-x)Pb(Mg1/3Nb2/3)O_3-xPbTiO_3$ single crystals, Scr. Mater. 69 (2013) 377.

[27] S. Zhang, S.M. Lee, D.H. Kim, H.Y. Lee, T.R. Shrout, Characterization of Mn-modified Pb(Mg(13)Nb(23))O(3)-PbZrO(3)-PbTiO(3) single crystals for high power broad bandwidth transducers, Appl. Phys. Lett. 93 (2008) 122908.

[28] S.J. Zhang, F. Li, F.P. Yu, X.N. Jiang, H.Y. Lee, J. Luo, T.R. Shrout, Recent developments in piezoelectric crystals, J. Korean Ceram. Soc. 55 (2018) 419.

[29] L.H. Luo, D. Zhou, Y.X. Tang, Y.M. Jia, H.Q. Xu, H.S. Luo, Effects of Mn doping on dielectric and piezoelectric properties of 0.71Pb(Mg1/3Nb2/3)O-3-0.29PbTiO(3) single crystals, Appl. Phys. Lett. 90 (2007) 102907.

[30] H.J. Lee, S. Zhang, T.R. Shrout, Scaling effects of relaxor-PbTiO(3) crystals and composites for high frequency ultrasound, J. Appl. Phys. 107 (2010) 124107.

[31] S. Zhang, F. Li, J. Luo, R. Sahul, T.R. Shrout, Relaxor-PbTiO3 single crystals for various applications, IEEE Trans. Ultrason. Ferroelectr. Freq. Control 60 (2013) 1572.
[32] H.J. Lee, S. Zhang, J. Luo, F. Li, T.R. Shrout, Thickness dependent properties of relaxor-PbTiO(3) ferroelectrics for ultrasonic transducers, Adv. Funct. Mater. 20 (2010) 3154.
[33] H.-T. Oh, H.-J. Joo, M.-C. Kim, H.-Y. Lee, Thickness-dependent properties of undoped and Mn-doped (001) PMN-29Pt [Pb(Mg1/3Nb2/3)O3-29PbTiO_3] single crystals, J. Korean Ceram. Soc. 55 (2018) 290.